Influence of Local Dynamical Air–Sea Feedback Process on the Hawaiian Lee Countercurrent

HIDEHARU SASAKI, BUNMEI TAGUCHI, AND NOBUMASA KOMORI

Earth Simulator Center, JAMSTEC, Yokohama, Kanagawa, Japan

YUKIO MASUMOTO

Research Institute for Global Change, JAMSTEC, Yokohama, Kanagawa, Japan

(Manuscript received 7 August 2012, in final form 11 March 2013)

ABSTRACT

Local air–sea interactions over the high sea surface temperature (SST) band along the Hawaiian Lee Countercurrent (HLCC) are examined with a focus on dynamical feedback of SST-induced wind stress to the ocean using the atmosphere–ocean coupled general circulation model (CGCM). A pair of ensemble CGCM simulations are compared to extract the air–sea interactions associated with HLCC: the control simulations and other simulations, the latter purposely eliminating influences of the high SST band on the sea surface flux computations in the CGCM. The comparison reveals that oceanic response to surface wind convergence and positive wind stress curl induced by the high SST band increases (decreases) the HLCC speed in the southern (northern) flank of the HLCC. The HLCC speed changes are driven by the Ekman suction associated with positive wind stress curl over the warm HLCC via the thermal wind balance. The HLCC speed increase is more significant than its decrease. This dynamical feedback is likely to be important to sustain the extension of the HLCC far to the west. The heat budget analysis confirms that advection of warm water from the west associated with this significant current speed increase plays a role in the southward shift of the HLCC axis. The dynamical feedback with the HLCC speed increase can potentially amplify the seasonal and interannual variations of HLCC.

1. Introduction

Local air–sea interactions associated with the oceanic fronts and mesoscale phenomena, which have significant potential impacts to regional and larger-scale climate systems, are observed in the World Ocean (see reviews of Small et al. 2008; Chelton and Xie 2010). Minobe et al. (2008) and Tokinaga et al. (2009) revealed that the Gulf Stream and Kuroshio Extension, respectively, affect not only the near-surface atmosphere but also the entire troposphere, suggesting an active role of the mid-latitude ocean in the weather and climate. Kobashi et al. (2008) also found a deep atmospheric response to the subtropical front, associated with the narrow eastward subtropical countercurrent in the North Pacific in spring. Furthermore, such atmospheric responses are shown to influence the oceanic condition in turn. Seo et al. (2007) revealed a negative feedback to the tropical instability wave (TIW) in the Atlantic that could dampen the growth rate of the TIW via influence of sea surface temperature (SST) on wind stress. Taguchi et al. (2012a), on the other hand, suggested that a positive air–sea feedback plays a role in sustaining the oceanic deep zonal jets through SST-induced finescale wind stress curls.

The Hawaiian Lee Countercurrent (HLCC; Qiu et al. 1997; Flament et al. 1998) provides another excellent opportunity to study local air–sea interactions associated with oceanic fronts in the extratropics. The HLCC is a narrow eastward countercurrent extending westward from Hawaii beyond the international date line, which is originally driven by orographic wind wake behind the Hawaiian Islands (Xie et al. 2001). Recent satellite observations revealed a zonal band of SST maximum along the HLCC and associated atmospheric responses with the surface wind convergence and distinct clouds over the warm current (Xie et al. 2001).

Corresponding author address: Hideharu Sasaki, Earth Simulator Center, JAMSTEC, 3173-25 Showa-machi, Kanazawa-ku, Yokohama, Kanagawa, 236-0001, Japan.
E-mail: sasaki@jamstec.go.jp

DOI: 10.1175/JCLI-D-12-00586.1

© 2013 American Meteorological Society

Following these atmospheric responses, thermal forcing onto the ocean, the wind-induced evaporation and shielding of downward shortwave radiation via clouds, have been suggested based on analyses of satellite observations (Xie et al. 2001). The atmospheric response and its thermal forcing onto the ocean have been confirmed to be operative in regional atmospheric model simulations (Hafner and Xie 2003).

In addition to the thermal forcing, dynamical feedbacks onto the ocean are expected to occur and are discussed in the following studies. The positive surface wind stress curl anomaly over the warm HLCC is inferred to drive ocean circulation by Sverdrup theory (Hafner and Xie 2003). Using a high-resolution ocean general circulation model (GCM), Sasaki and Nonaka (2006) suggested the importance of local wind convergence over the warm HLCC and associated dynamical feedback processes in the far-extending HLCC system. Using an atmospheric–ocean coupled GCM (CGCM), Sakamoto et al. (2004) succeeded in reproducing the far-extending HLCC and confirmed that the Hawaiian Islands are key to trigger the simulated HLCC accompanied by the air–sea interactions. While all these studies conjectured the importance of air–sea interaction in maintaining the HLCC, detailed mechanisms, particularly the dynamical feedbacks on to the ocean and their influences on the HLCC are yet to be explicitly demonstrated.

This study, therefore, examines how the local atmospheric responses over the warm HLCC in turn influence the oceanic field using a CGCM. In addition to ensemble control simulations with atmospheric perturbations, we have conducted another set of ensemble simulations, in which influence of the warm SST band on surface heat and momentum flux computations in the CGCM is purposely excluded. A comparison of results from the two sets of ensemble simulations is expected to reveal the air–sea interactions associated with the high SST band. Influence of the air–sea interactions on oceanic temperature field is also examined. The rest of the paper is organized as follows. In section 2, the CGCM used in the present study and ensemble simulations is described. Section 3 shows the local air–sea interactions induced by the warm HLCC in the CGCM. In section 4, influences of the dynamical feedback on the HLCC system are discussed and conclusions are offered.

2. CGCM simulations

a. Model and observation data

The model used in this study is the CGCM for the Earth Simulator (CFES, Komori et al. 2008), which consists of the Atmospheric GCM for the Earth Simulator (AFES; Ohfuchi et al. 2004; Enomoto et al. 2008; Kuwano-Yoshida et al. 2010) and the Oceanic GCM for the Earth Simulator (OFES; Masumoto et al. 2004; Komori et al. 2005). The AFES is based on the Center for Climate System Research (CCSR)/National Institute for Environmental Studies (NIES) atmospheric GCM 5.4.02 (Numaguti et al. 1997), and the OFES is based on the Modular Ocean Model version 3 (MOM3; Pacanowski and Griffies 1999).

The wind stress product at a resolution of 0.5° based on Quick Scatterometer (QuikSCAT) satellite observations was obtained from the Japanese Ocean Flux Datasets with the Use of Remote Sensing Observations product (J-OFURO; Kutsuwada 1998; Kubota et al. 2002). SST from the Tropical Rainfall Measuring Mission (TRMM) satellite (Wentz et al. 2000) and sea surface height (SSH) of Maps of the Absolute Dynamic Topography (MADT) from Archiving, Validation, and Interpretation of Satellite Oceanographic data (AVISO; http://www.aviso.oceanobs.com) at a horizontal resolution of 0.25° were also used.

b. Control and no warm SST band ensemble simulations

The CFES integration analyzed in this study is a simulation at a horizontal resolution of T119 (~1°) and 48 vertical levels in the atmosphere, and 0.5° horizontal resolution and 54 vertical levels in the ocean (Richter et al. 2010; Taguchi et al. 2012b). The reference simulation has been carried out for 150 years starting 1 January of the climatological atmospheric conditions of the 40-yr European Centre for Medium-Range Weather Forecasts (ECMWF) Re-Analysis (ERA-40; Uppala et al. 2005) and the oceanic conditions of the temperature and salinity fields from the *World Ocean Atlas 1998* (*WOA98*; Antonov et al. 1998a,b,c; Boyer et al. 1998a,b,c) without motion.

The simulated HLCC in the reference simulation exhibits seasonal variations, strong from summer to winter and weak in spring as observed (Kobashi and Kawamura 2002; Sasaki et al. 2010), and interannual variations (Sasaki et al. 2012) (not shown). We focus on the simulated HLCC and the associated air–sea interactions in the summer (from July to September) of the 115th year. In this period, the HLCC with distinct high SST band extends farther to the west than in other years, and the wind stress convergence over the warm HLCC is prominent (Fig. 1a). Compared with the satellite observations when the HLCC extended far to the west in the summer of 2003 (Fig. 1b), the simulated HLCC does not extend farther west and the wind stress convergence is weak. The HLCC speed away from Hawaii

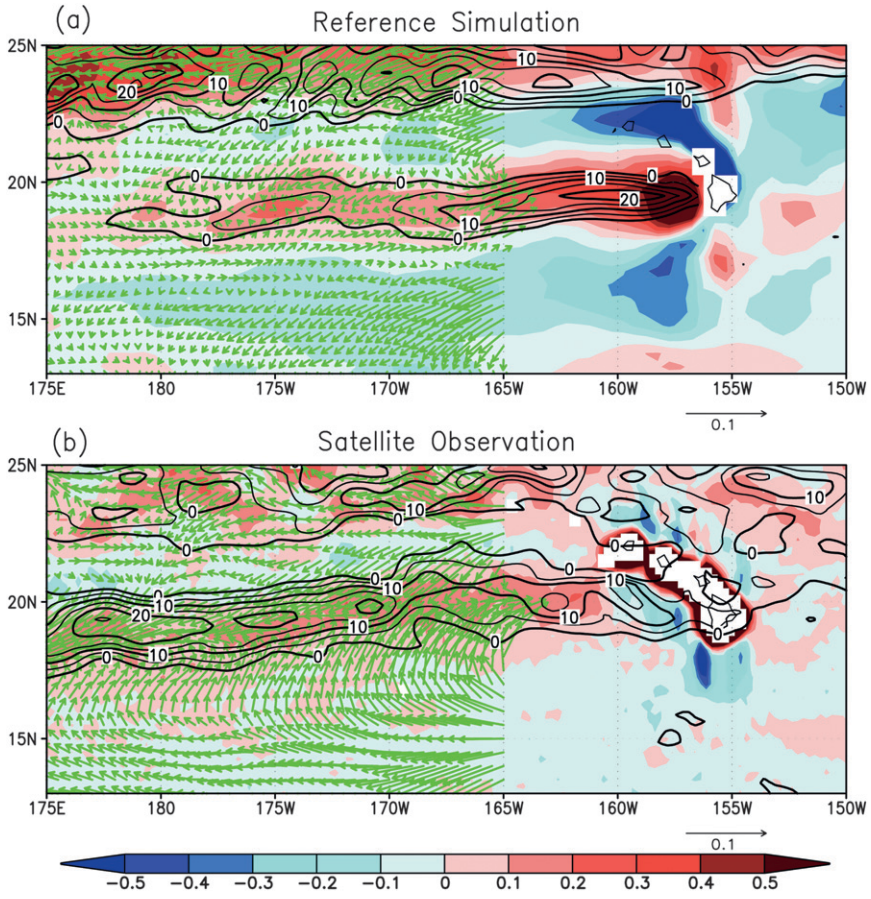

FIG. 1. Meridional high-pass filter via removing an 8° moving mean is applied to SST and wind stress; geostrophic eastward current speed (contour, cm s^{-1}), SST (color, °C), and wind stress vectors (10^{-1} N m^{-2}). (a) Mean in the summer of the 115th year in the reference simulation and (b) mean in the summer of 2003 in the satellite observations of geostrophic current based on the SSH from AVISO, SST from TRMM satellite, and wind stress from QuikSCAT satellite observations. Contour intervals are 5 cm s^{-1}. Wind stress vectors are shown to the west of 165°W.

is low in the model (>5 cm s^{-1}) than in the observations (>15 cm s^{-1}), although the HLCC speed is high (>20 cm s^{-1}) near Hawaii (Fig. 1).

We conducted control ensemble simulations [hereafter referred to as the control (CNTL) simulations] in the summer of the 115th year. The ensemble consists of 5 members: one performed with the 1 July initial condition taken from the reference simulation, and the other four with the same oceanic initial condition whereas atmospheric fields replaced with the outputs of the reference simulation on 29 and 30 June and 2 and 3 July, respectively.

In the summer of the 115th year, the SST in the reference simulation becomes higher along the HLCC than that of surrounding water (Fig. 2). Other ensemble simulations removing the influence of the warm SST band on heat and momentum fluxes in the CGCM have been conducted from July to September in the 115th year [hereafter referred to as the no warm SST band (NWSB) simulations]. In the NWSB simulations, the heat and momentum fluxes in the rectangular region around the HLCC (15°–23°N, 180°–165°W) are estimated at each time step using the SST smoothed by 8°-wide meridional running means. Differences in ensemble means between the CNTL and NWSB simulations are expected to show contributions of the high SST peak to local air–sea interactions away from Hawaii. Considering the influence of atmospheric natural variability, the statistical significance of the differences is estimated using two-sided Student's *t* test.

3. Results

a. Atmospheric response to high SST band

Atmospheric responses induced by the high SST peak along the HLCC are examined by comparing ensemble-mean atmospheric fields between the CNTL and NWSB

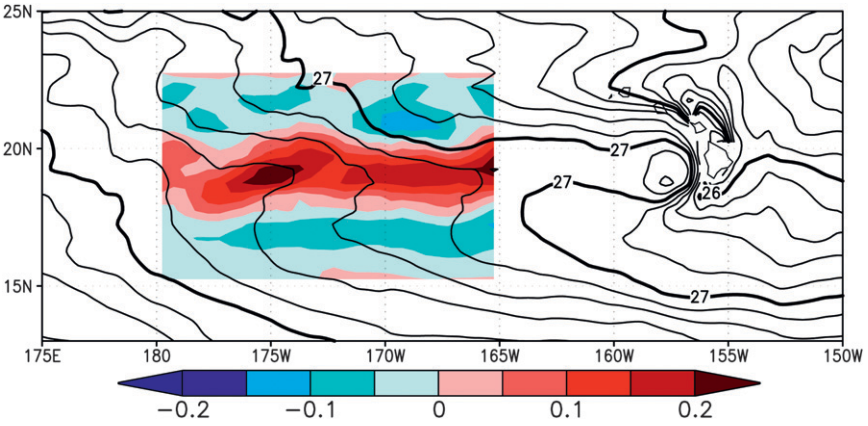

FIG. 2. SST (contour, °C) in the summer of the 115th year in the reference simulation. Color is the difference between SST in the reference simulation and that smoothed in the rectangular region (15°–23°N, 180°–165°W) by replacing with the meridional running means (SST in the reference simulation − smoothed SST).

simulations (hereafter, the ensemble mean fields of each respective simulations are referred to as simply the CNTL and NWSB simulations). The ensemble mean difference in wind stress fields exhibits a zonal band of convergence toward the high SST peak between 175° and 160°W and its strong positive curl ($>2 \times 10^{-8}\,\mathrm{N\,m^{-3}}$) west of 165°W along approximately 19°N (Fig. 3). The positive wind stress curl is produced by the southwestward wind stress to the north and northeastward wind stress to the south with the Coriolis and pressure gradient forces roughly balanced each other. This wind stress curl difference is statistically significant at the 90% confidence level. Cumulus clouds are also more prominent over the warm HLCC in the CNTL simulations than in the NWSB simulations (not shown). These atmospheric responses to the high SST have been detected in the satellite observations (Xie et al. 2001).

We next look into what mechanisms are responsible for the near-surface wind response to the underlying high SST band. It is found that the difference of wind convergence ($>4 \times 10^{-7}\,\mathrm{s^{-1}}$) between the CNTL and NWSB simulations is spatially best correlated with that of the positive SLP Laplacian ($>0.6 \times 10^{-10}\,\mathrm{Pa\,m^{-1}}$) along 19°N to the west of 165°W (Fig. 4). This relationship is consistent with the pressure adjustment mechanism in the atmospheric boundary layer (ABL) (e.g., Lindzen and Nigam 1987), whereby the pressure anomalies produce wind convergence over the warm SST (e.g.,

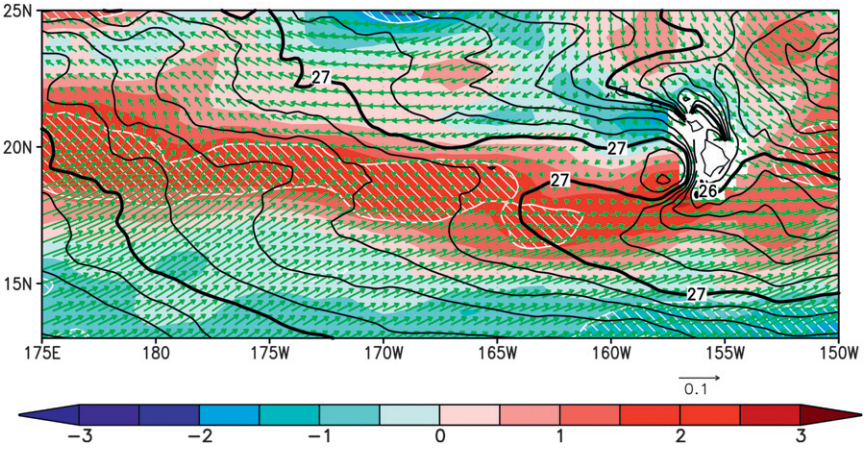

FIG. 3. Ensemble mean difference of wind stress vectors ($10^{-1}\,\mathrm{N\,m^{-2}}$) and curl (color, $10^{-8}\,\mathrm{N\,m^{-3}}$) in the summer of the 115th year between the CNTL and NWSB simulations (CNTL − NWSB). Black contours indicate SST in the CNTL simulation. The hatched region is where the *t*-test significance is higher than 0.9.

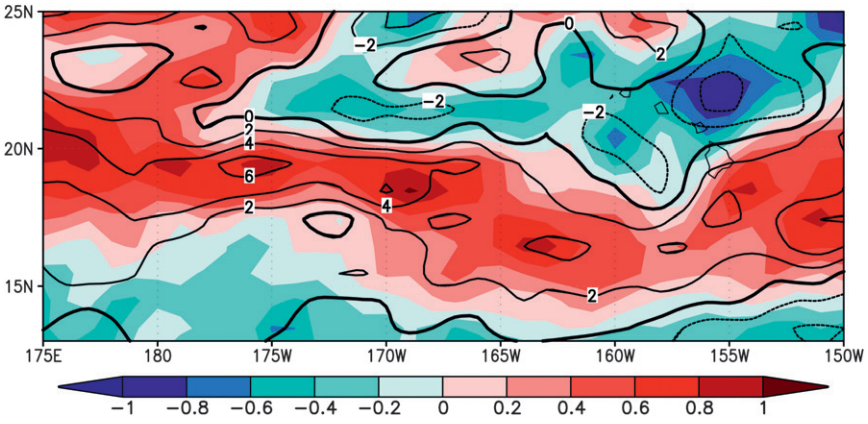

FIG. 4. Ensemble mean difference of SLP Laplacian (color, 10^{-10} Pa m^{-3}) and 10-m wind convergence (contour, 10^{-7} s^{-1}) in the summer of the 115th year between the CNTL and NWSB simulations (CNTL − NWSB).

Minobe et al. 2008; Shimada and Minobe 2011). The strength of this ABL response can be measured with the linear slope between the SST Laplacian and wind convergence (Shimada and Minobe 2011). In the reference simulation in the summer of the 115th year, the slope is estimated as 4.7×10^4 m^2 °C^{-1} s^{-1} in the HLCC region. Interestingly, the air–sea coupling is larger than that in the western boundary current (WBC) regions (e.g., 9.8×10^3 m^2 °C^{-1} s^{-1} in the Agulhas Return Current region), although the SST Laplacian in the HLCC region ($\sim 10^{-11}$ °C m^{-2}) is much smaller than in the WBC region ($\sim 10^{-10}$ °C m^{-2}). This strong air–sea coupling in the HLCC region is presumably due to the enhanced surface wind convergence induced by active convection and its associated latent heat release over the warm subtropical ocean. The comparison between the coupling magnitudes in the CGCM and observations is discussed in detail in the appendix.

For the dynamical effect of the perturbation wind stress on the ocean, the Ekman divergence and thus the difference of wind stress curl over the high SST band along the HLCC (Fig. 3) is important, which also seems to be induced by the pressure adjustment mechanism of the ABL in the CGCM. Based on the simple ABL model (Lindzen and Nigam 1987; Minobe et al. 2008), Taguchi et al. (2012a) showed that the wind curl is associated with the wind convergence under the effect of Coriolis force and the surface friction, leading to the in-phase relationship between SST Laplacian and wind curl [see their Eq. (3)]. The linear slope between the latter two in the summer of the 115th year in the reference simulation (4.6×10^4 m^2 °C^{-1} s^{-1}) is comparable to that between the SST Laplacian and wind convergence. Although the SST along the HLCC is higher by only 0.2°C than the surrounding water (Fig. 2), the ABL response over the warm ocean around the HLCC induces not only wind convergence but also the distinct wind curl over the current.

Besides the pressure adjustment mechanism, the vertical mixing mechanism is another well-known ABL response to SST anomalies (e.g., Wallace et al. 1989). However, the relationships between the downwind SST gradient and wind stress convergence and between the crosswind SST gradient and wind stress curl are unclear in the reference simulation (not shown). This is presumably because these relationships suggesting the vertical mixing mechanism are masked in the HLCC region by the alternative effect of the pressure adjustment mechanism, which can be enhanced by the active convection over the warm subtropical ocean and the associated latent heat release. What determines the mode of ABL response to finescale SST anomalies in the HLCC and other regions should be explored in further studies.

b. *Dynamical feedback to the ocean and its influence on the HLCC*

To examine dynamical feedback of the SST-induced wind stress to the ocean and its influence on the HLCC, oceanic fields in the CNTL and NWSB simulations are compared. To the west of 165°W, the eastward surface current speed of the CNTL simulations is higher (lower) to the south (north) of HLCC axis than that of the NWSB simulations (Fig. 5), which suggests the HLCC speed changes as a result of the dynamical feedback to the ocean. In the southwest of HLCC around 175°W where the maximum speed is about 8 cm s^{-1} in the CNTL simulations, the current speed increases by more than 1.5 cm s^{-1}, which is statistically significant at more than 90% confidence level. On the other hand, the current speed decrease to the north of HLCC is less significant.

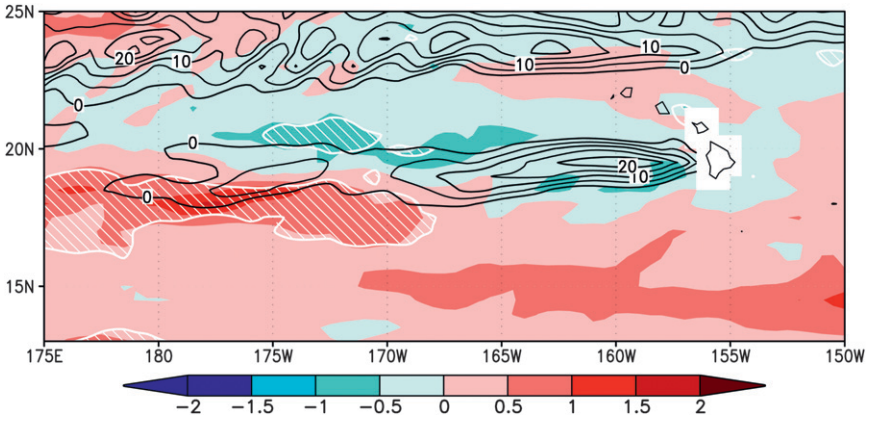

FIG. 5. Ensemble mean difference of eastward surface current speed (cm s^{-1}) in the summer of the 115th year between the CNTL and NWSB simulations (CNTL − NWSB). Black contours indicate eastward current speed in the CNTL simulation. Contour intervals are 5 cm s^{-1}. The hatched region is where the *t*-test significance is higher than 0.9.

The zonal mean profile of eastward surface current speed averaged between 180° and 170°W also confirms the HLCC speed increase (decrease) to the south (north) of HLCC axis: 1.7 cm s^{-1} (0.3 cm s^{-1}) in the CNTL simulations and 0.8 cm s^{-1} (0.7 cm s^{-1}) in the NWSB simulations along 18.5°N (20°N) (Fig. 6a). Near Hawaii (165°–160°W), however, the surface current profiles in both the simulations are almost the same (Fig. 6b). These changes in the HLCC speed represent the slight southward shift away from Hawaii in the CNTL simulations relative to the NWSB simulations. The HLCC speed change with significant increase in the south could influence on the current path, which is discussed in detail in section 4.

Figure 7 shows latitude–depth sections of potential density and eastward current speed averaged between 180° and 170°W. In the CNTL simulations, the depth of the mixed layer is approximately 35 m (Fig. 7a), and the isopycnals in the density range around 23.2σ_θ slope up northward between 18° and 20°N and sharply stratified around 20°N at a depth of approximately 50 m. The eastward current, corresponding to the HLCC, is located at around 19°N in the upper ocean from the sea surface to 90-m depth, with a core speed higher than 6 cm s^{-1} at a depth of approximately 30 m (Fig. 7b).

The eastward current speed in the upper layer above 90 m depth is higher (lower) in the southern (northern) part of the HLCC in the CNTL simulations than in the NWSB simulations (Fig. 7b). The current speed increase south of HLCC axis between 17.5° and 18.5°N is large (>0.8 cm s^{-1}) and statistically significant at more than 90% confidence level. On the other hand, the current decrease north of the HLCC axis is relatively small (<−0.6 cm s^{-1}) and less significant at the depth shallower than 20 m. The significant HLCC speed increase should help the HLCC extend farther to the west and be sustained. This result supports the hypothesis proposed by an OGCM study (Sasaki and Nonaka 2006) that the local wind convergence over the warm SST band further drives the HLCC.

The isopycnals centered around 23.2σ_θ are shallower at 19°N, and their slopes are steeper (more gradual) to the south (north) in CNTL simulations than in the NWSB simulations (Fig. 7a). The positive difference in potential density around 19°N at the depth deeper than 60 m is largely significant. In the mixed layer, a pair of positive and negative differences appears to the north and south, respectively, of the core of the HLCC in the CNTL simulations (~19°N). Warm (cold) water advection from the west (east) by the current speed difference (Fig. 7b) seems to contribute to these density differences.

c. *Mechanism of the HLCC speed change by dynamical feedback*

To see the mechanism of dynamical feedback with the HLCC speed change, the response of pycnocline depth to the wind convergence over the warm HLCC is examined. The depth difference of isopycnal surface of 23.2σ_θ, corresponding to the typical pycnocline (Fig. 7a) between the CNTL and NWSB simulations is large (>1.2 cm) and statistically significant at 90% confidence level between 176° and 172°W along 19°N (Fig. 8). This large difference of pycnocline displacement roughly corresponds to the displacement induced by Ekman suction via wind stress difference between the CNTL and NWSB simulations (Fig. 8). This correspondence shows that the positive wind stress curl of atmospheric

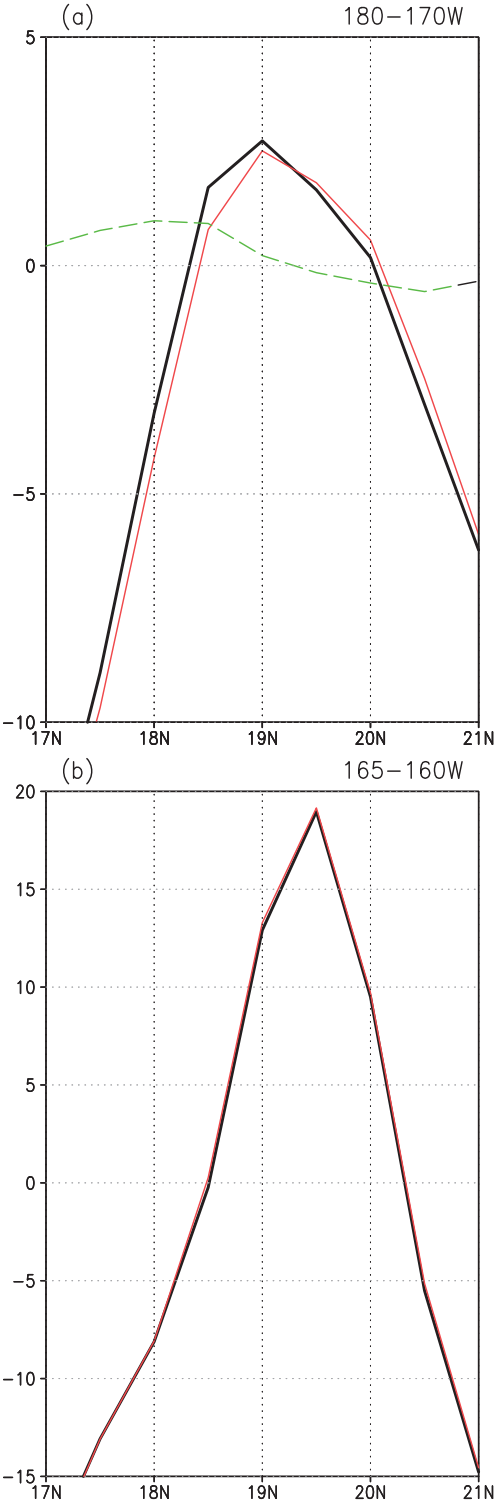

FIG. 6. Ensemble mean eastward current speeds (cm s^{-1}) at sea surface averaged (a) between 180° and 170°W and (b) between 165° and 160°W in the CNTL (black curves) and NWSB (red curves) simulations in the summer of the 115th year. Green dashed curve in (a) indicates the ensemble mean difference of eastward current speeds between the CNTL and NWSB simulations (CNTL − NWSB).

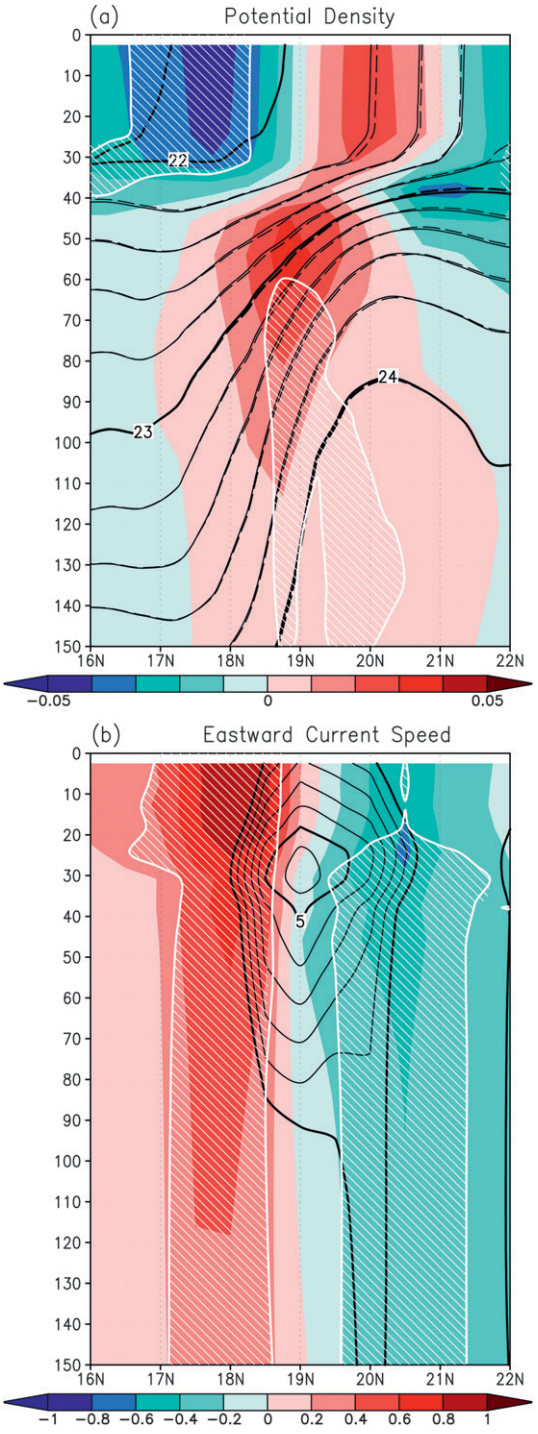

FIG. 7. Latitude–depth sections averaged between 180° and 170°W in the summer of the 115th year. (a) Ensemble mean potential density (σ_θ) in the CNTL (solid curve) and NWSB (dashed curve) simulations. Color indicates the difference of ensemble mean potential density (CNTL − NWSB). (b) Ensemble mean difference of eastward current speed (color, cm s^{-1}) (CNTL − NWSB). Contours indicate the ensemble mean eastward current speed (>0 cm s^{-1}) in the CNTL simulations with intervals of 1 cm s^{-1}. The hatched region is where the *t*-test significance is higher than 0.9.

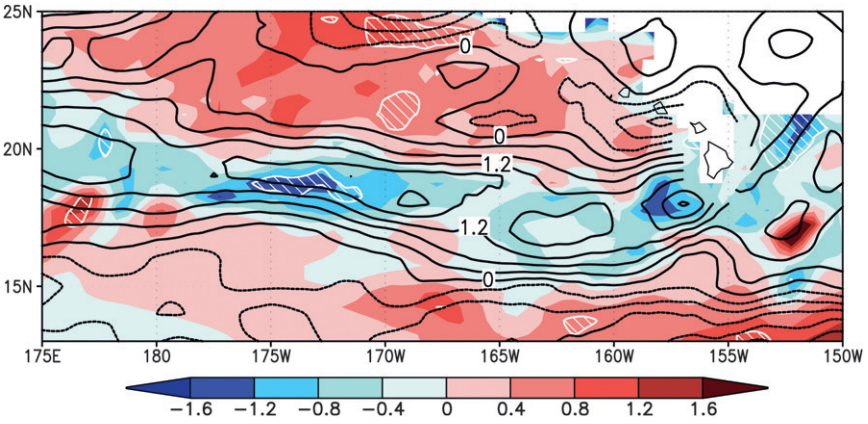

FIG. 8. As in Fig. 5, but the color is the ensemble mean difference (CNTL − NWSB) of the $23.2\sigma_\theta$ isopycnal surface depth (m) and contours indicate vertical displacements (m) via Ekman pumping forced by wind stress difference. Based on the finite difference method, the mean displacement corresponds to that for 1.5 month via Ekman pumping velocity averaged in the summer. The Ekman pumping velocity is defined as $\mathrm{curl}(\Delta\tau/f)/\rho$, where $\Delta\tau$ is the ensemble mean difference of the wind stress vector, f is the Coriolis parameter, and ρ is the water density. The hatched region is where the t-test significance is higher than 0.9.

response (Fig. 3) lifts the pycnocline via Ekman suction. Maximum meridional gradient of the pycnocline displacement between 180° and 170°W is about -1.0×10^{-7} (0.8×10^{-7}) to the south (north) of the HLCC, which could induce the current speed increase of $1.0\,\mathrm{cm\,s^{-1}}$ (decrease of $0.8\,\mathrm{cm\,s^{-1}}$) based on the thermal wind balance. Therefore, the HLCC speed increase ($>0.8\,\mathrm{cm\,s^{-1}}$) around 18°N and decrease ($<0.6\,\mathrm{cm\,s^{-1}}$) around 20.5°N (Fig. 7b) are consistent with the thermal wind balance of the pycnocline slope change (Fig. 7a). The large differences in both the pycnocline depth and displacement via Ekman suction can also be found outside of the region with the smoothed SST in the NWSB simulations. These signals, however, are not statistically significant.

d. Influence of local feedbacks on ocean temperature

In this section, how both the local thermal and dynamical feedbacks influence the ocean temperature field around the HLCC is examined. In the region from 180° to 165°W where the air–sea coupling is partially disabled in the NWSB simulations, the SST is broadly higher to the south and lower to the north of HLCC in the CNTL simulations than in the NWSB simulations (Fig. 9). Around the HLCC, there are a pair of statistically significant differences in SST peaks, with the positive peak

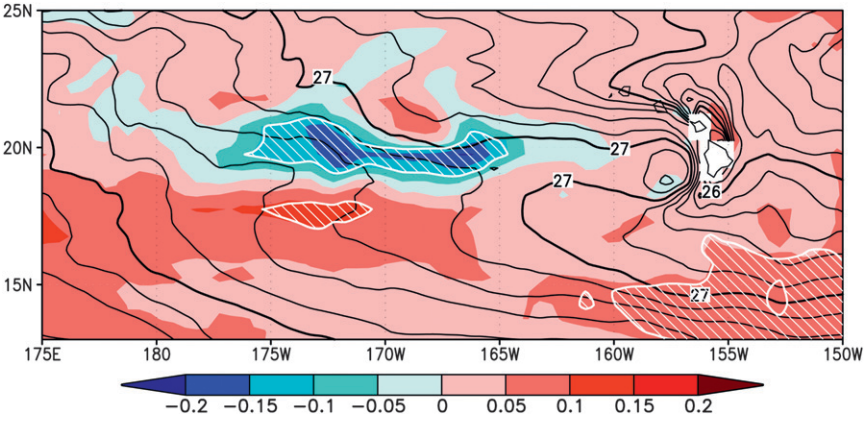

FIG. 9. As in Fig. 5, but the color is the ensemble mean SST (°C) difference (CNTL − NWSB) between the CNTL and NWSB simulations, and contours indicate SST in the CNTL simulation with intervals of 0.2°C. The hatched region is where the t-test significance is higher than 0.9.

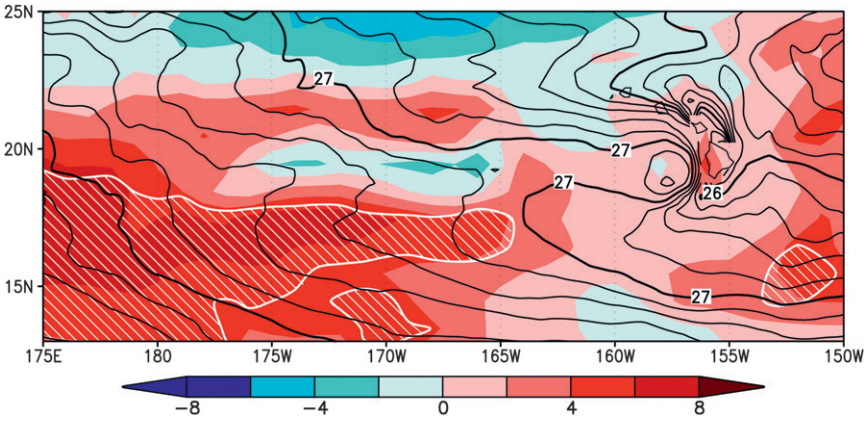

FIG. 10. Ensemble mean difference of latent heat flux (color, $W m^{-2}$) in the summer of the 115th year between the CNTL and NWSB simulations (CNTR − NWSB). Contours indicate SST in the CNTL simulation. The hatched region is where the *t*-test significance is higher than 0.9.

between 175°E and 170°W along 17.5°N (>0.1°C) and the negative peak between 173° and 165°W along 20°N (<0.15°C).

The surface heat flux difference between the CNTL and NWSB simulations averaged in the summer of the 115th year is examined. The easterly trade winds are strengthened to the north and weakened to the south of HLCC by the southwestward and northeastward wind stress differences, respectively (Fig. 3), which are induced by the high SST band. As a result, surface cooling via evaporation becomes correspondingly large ($<-2\,W m^{-2}$) to the north and small ($>6\,W m^{-2}$) to the south (Fig. 10), which are consistent with those in Xie et al. (2001) and Hafner and Xie (2003). The small (large) surface cooling to the south along 17°N (north along 19.5°N) is significant (nonsignificant). The reason why the significance of the north is degraded is still unclear, which should be examined in the future.

The shielding of downward shortwave radiation by clouds also appears to influence the SST locally along the HLCC. Downward shortwave radiation over the HLCC is lower ($<-4\,W m^{-2}$) approximately along 19.5°N to the west of 170°W in the CNTL simulations than in the NWSB simulations (Fig. 11) due to more prominent cumulus clouds over the HLCC in the CNTL simulations (not shown). These two thermal feedbacks to the ocean have not been explicitly demonstrated until the present study, while their influences on the SST were suggested in previous studies (Xie et al. 2001; Hafner and Xie 2003).

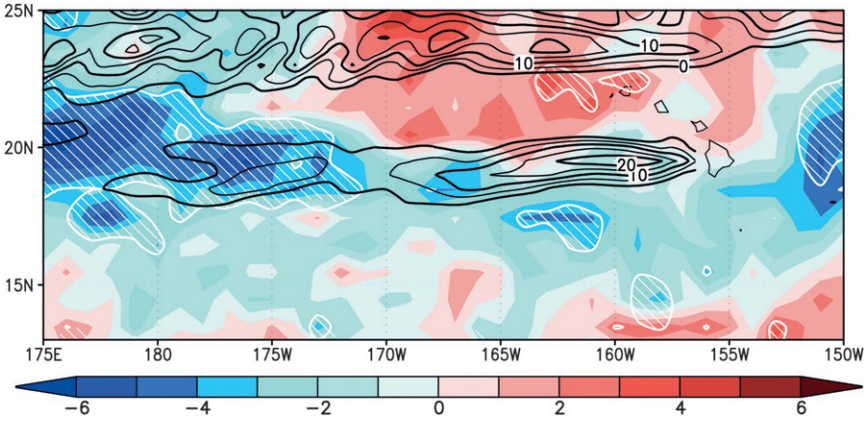

FIG. 11. As in Fig. 5, but the color is the ensemble mean difference (CNTL − NWSB) of downward shortwave radiation ($W m^{-2}$) at the sea surface between the CNTL and NWSB simulations, and contours indicate the eastward current speed at sea surface in the CNTL simulation with the contour interval of $5\,cm\,s^{-1}$. The hatched region is where the *t*-test significance is higher than 0.9.

In addition to these thermal feedbacks, the HLCC speed increase of dynamical feedback could influence the SST via warm (cold) water advection from the west (east) in the south (north) of HLCC. The significant positive (negative) zonal current speed difference (Fig. 5) and positive (negative) SST difference (Fig. 9) are to some degree collocated each other in the south (north) of HLCC.

To examine what mechanism is important to temperature field around the HLCC, we have monitored heat budget terms in the mixed layer both in the CNTL and NWSB simulations. The change rate of the mixed layer temperature is defined as

$$\frac{\partial T_{\mathrm{mix}}}{\partial t} = \frac{Q}{\rho C_p H_{\mathrm{mix}}} - \frac{1}{H_{\mathrm{mix}}} \int_{-H_{\mathrm{mix}}}^{0} (\mathbf{U} \cdot \nabla T)\, dz + \text{residual}, \tag{1}$$

where T and T_{mix} are the potential temperature and its mean value throughout the mixed layer, respectively; Q is the surface heat flux minus penetrating shortwave radiation flux through the bottom of mixed layer; ρ is the water density; C_p is the heat capacity; H_{mix} is the mixed layer thickness; and $\mathbf{U}$ is the current velocity vector. The depth of mixed layer bottom is defined as the depth at which potential density differs from the sea surface density by $0.125\sigma_\theta$. The left side of this equation represents the change rate of the mixed layer temperature. The first term on the right side is the resultant heating from vertical convergence of heat fluxes, the second term is the heat advection term in the mixed layer, and the third term is the residual.

Figure 12 shows the meridional profile of each term difference of 180°–170°W between the CNTL and NWSB simulations averaged for the summer of the 115th year. Tendency of the mixed layer temperature agrees well with the SST difference at the end of the summer. The residual term, which mostly represents vertical diffusion, does not have much influence on the temperature change. The large positive heat advection difference at around 18°–19°N (>0.05°C month^{-1}) is located slightly to the south of the negative surface heating difference (<0.05°C month^{-1}) at around 19°N. This heat advection and the surface heating (>0.05°C month^{-1}) to the south of 18°N contribute to the positive difference of mixed layer temperature to the south of 18°N. To the north of 20°N, the negative difference of heat advection also causes the negative difference of mixed layer temperature, although its contribution is relatively small compared to that in the south. These results show that not only the surface heating via thermal feedbacks, but also the heat advection via dynamical feedback,

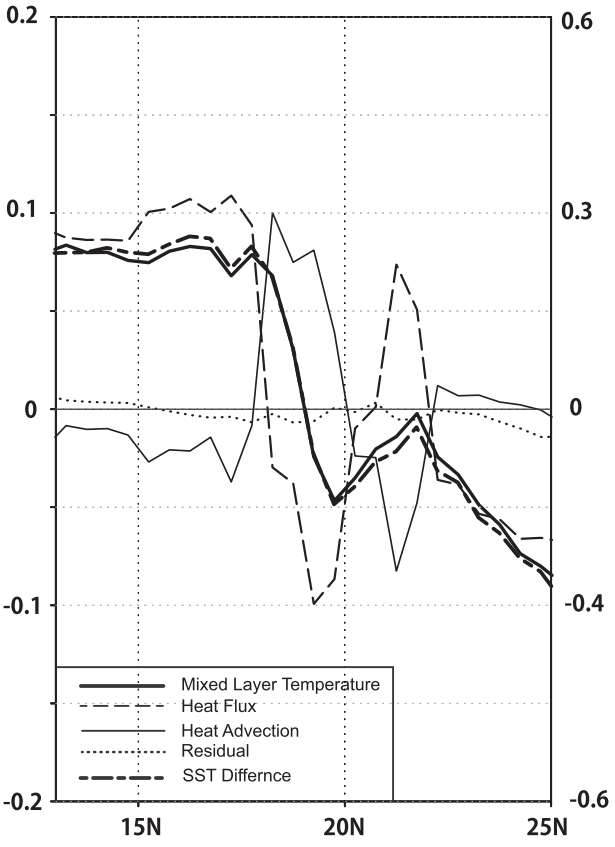

FIG. 12. Change rates differences (°C month^{-1}) in the mixed layer averaged from 180° to 170°W in the summer of the 115th year between ensemble means of the CNTL and NWSB simulations (CNTL − NWSB). Mixed layer potential temperature (thick solid curve), term of surface heating minus permeation flux at bottom of the mixed layer (dashed curve), heat advection term in the mixed layer (thin solid curve), and residual (dotted curve). Dashed–dotted line indicates the SST difference at the end of the summer.

contribute to the change rate of temperature locally around the HLCC. Significances of the current speed difference (Fig. 5) and latent heat flux difference (Fig. 10) in the south of HLCC support that both of the warm water advection and surface heating contribute the mixed layer warming in the south of the HLCC. These results suggest that the both thermal and dynamical feedbacks play roles in the southward shift of the warm SST band associated with the HLCC.

4. Conclusions and discussion

The present study examines local air–sea interactions induced by the high SST band along the HLCC in the CGCM simulations, with a focus on dynamical feedback to the ocean. A comparison of ensemble mean results from the CNTL simulations and NWSB simulations in which influence of the high SST peak is eliminated

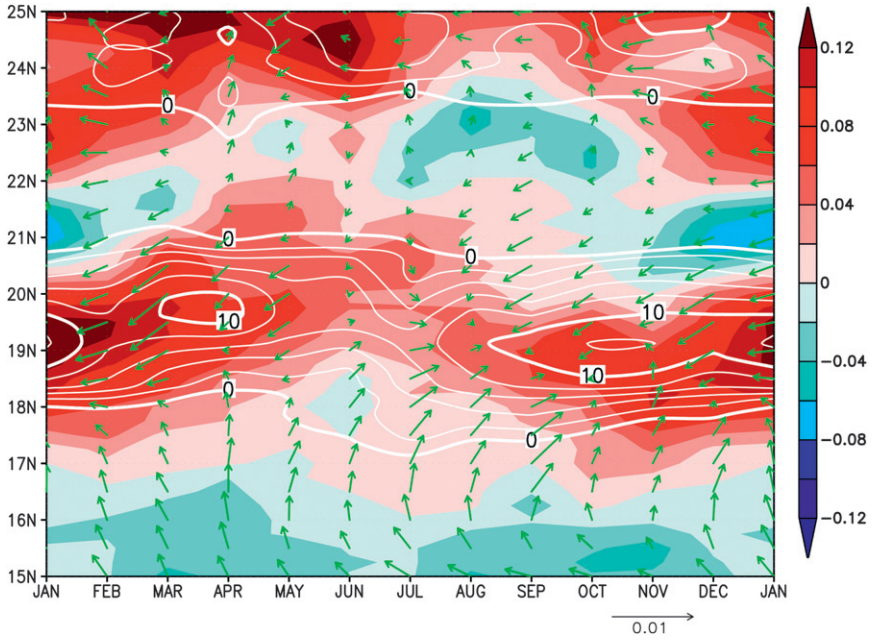

FIG. 13. Seasonal march of the wind stress vector (N m^{-2}), SST (color, °C), and geostrophic zonal current (>0 cm s^{-1}) (contour, cm s^{-1}) averaged from 180° to 170°W based on QuikSCAT, TRMM, and AVISO satellite observations, respectively. Meridional high-pass filter via removing an 8° running mean is applied to the wind stress and SST. Contour intervals are 2 cm s^{-1}.

reveals that atmospheric response to the SST peak in turn increases (decreases) the current speed in the southern (northern) part of HLCC. Ekman suction by positive wind stress curl over the warm HLCC is responsible for these HLCC speed changes based on the thermal wind balance. In addition, the warm and cold water advections by this HLCC speed changes influence the temperature around the HLCC. The significant HLCC speed increase with warm water advection through the dynamical feedback is likely to be important to sustain the extension far to the west and the southward shift of the HLCC.

This study suggests that the dynamical feedback of significant HLCC speed increase with warm water advection plays a role in the meridional shift of the HLCC. On the other hand, the previous studies implied that the high SST band along the HLCC tends to move southward via thermal feedback into the ocean (Xie et al. 2001; Halner and Xie 2003). In addition, other mechanisms such as the influence from background flow (Maximenko et al. 2008) may contribute the meridional position of zonal current. Future studies are necessary to examine what mechanism is important in the HLCC tilting.

Moreover, it is also possible that the HLCC speed increase due to the dynamical feedback plays a role in the seasonal (Kobashi and Kawamura 2002; Sasaki et al. 2010) and interannual (Sasaki et al. 2012) variations of HLCC. In the case of seasonal variations, the satellite observations show that when the HLCC is strong from October to March between 180° and 170°W, both high SST peak and wind convergence are prominent at the latitude of the HLCC (Fig. 13). The SST along the HLCC rises because of the large advection of warm water from the west, and the subsequent atmospheric response with the wind convergence to the high SST peak becomes strong. Furthermore, the HLCC speed is expected to increase via the significant dynamical feedback in the south of HLCC forced by the strong atmospheric response. Therefore, the dynamical feedback may amplify the HLCC variations in the seasonal and similarly in the interannual time scales.

The dynamical feedback suggested in the present study may influence mesoscale eddies. For example, the vertical structure change in the thermoclines along the HLCC (Fig. 7a) may influence eddy activities along the HLCC via vertical shear change (Yoshida et al. 2011). Since the CFES at a horizontal resolution of 0.5° in the ocean used in this study cannot resolve mesoscale eddies, further studies are necessary using the CGCM with the finer resolution.

We evaluated the statistical significance of our results only for the summer of the 115th year. However, intrinsic variability in other years could be different from that in this specific summer. In addition, we have not examined how the local air–sea interactions influence remotely the wider areas. To address these issues, ensemble simulations with larger members should be conducted. These further studies are necessary steps for better understanding of the role of local air–sea interactions revealed in the present study. It is of great interest to investigate whether the dynamical feedback onto the current speed elucidated in this study is operative not only for the HLCC but also for other currents with SST front such as the western boundary currents. The comparison of CGCM simulations demonstrated in this study to extract the dynamical feedback provides a useful method to conduct this future work.

Acknowledgments. The CFES simulations were conducted on the Earth Simulator under support from JAMSTEC. We thank Profs. T. Yamagata, T. Hibiya, H. Nakamura, M. Watanabe, and H. Hasumi for valuable discussions. QuikSCAT wind stress data in the J-OFURO dataset were provided by Prof. K. Kutsuwada. This work is partially supported by MEXT/JST KAKENHI (HS and BT: 22106006 and 23340139, BT: 24540476, NK: 22106008 and 22244057).

APPENDIX

Air–Sea Coupling Strength in CGCM and Observation

We have examined the air–sea coupling magnitude in the reference simulation compared with that in Shimada and Minobe (2011), who quantified the strength of the ABL response to SST anomalies via the pressure adjustment mechanism with the linear relation between Laplacians of SST and lower tropospheric air thickness corresponding to SLP [$s(\Delta\text{SST}, \Delta H)$] and that between the thickness Laplacian and wind convergence [$s(\Delta H, \text{convU})$] using the satellite sounding and scatterometer. Since the simulated SLP field in the CFES is contaminated by the spectral noise by Gibbs phenomena, we estimate the linear slope between SST Laplacian and wind convergence [$s(\Delta\text{SST}, \text{convU})$]. Although Shimada and Minobe (2011) did not directly examine this quantity, it can be inferred by multiplying the two directly estimated quantities together [i.e., $s(\Delta\text{SST}, \text{convU}) = s(\Delta\text{SST}, \Delta H) \times s(\Delta H, \text{convU})$]. In the WBC region, the annual mean slope (about $1 \times 10^4\,\text{m}^2\,^\circ\text{C}^{-1}\,\text{s}^{-1}$) in the reference simulation for 6 years from the 115th to 120th year is comparable to the estimation from the climatological annual mean based on observations for 6 years (Shimada and Minobe 2011).

REFERENCES

Antonov, J. I., S. Levitus, T. P. Boyer, M. E. Conkright, T. O'Brien, and C. Stephens, 1998a: *Temperature of the Atlantic Ocean.* Vol. 1, *World Ocean Atlas 1998,* NOAA Atlas NESDIS 27, 166 pp.

——, ——, ——, ——, ——, and ——, 1998b: *Temperature of the Pacific Ocean.* Vol. 2, *World Ocean Atlas 1998,* NOAA Atlas NESDIS 28, 166 pp.

——, ——, ——, ——, ——, ——, and B. Trotsenko, 1998c: *Temperature of the Indian Ocean.* Vol. 3, *World Ocean Atlas 1998,* NOAA Atlas NESDIS 29, 166 pp.

Boyer, T. P., S. Levitus, J. I. Antonov, M. E. Conkright, T. O'Brien, and C. Stephens, 1998a: *Salinity of the Atlantic Ocean.* Vol. 4, *World Ocean Atlas 1998,* NOAA Atlas NESDIS 30, 166 pp.

——, ——, ——, ——, ——, and ——, 1998b: *Salinity of the Pacific Ocean.* Vol. 5, *World Ocean Atlas 1998,* NOAA Atlas NESDIS 31, 166 pp.

——, ——, ——, ——, ——, ——, and B. Trotsenko, 1998c: *Salinity of the Indian Ocean.* Vol. 6, *World Ocean Atlas 1998,* NOAA Atlas NESDIS 32, 166 pp.

Chelton, D. B., and S.-P. Xie, 2010: Coupled ocean-atmosphere interaction at oceanic mesoscales. *Oceanography,* **23** (4), 52–69.

Enomoto, T., A. Kuwano-Yoshida, N. Komori, and W. Ohfuchi, 2008: Description of AFES 2: Improvements for high-resolution and coupled simulations. *High Resolution Numerical Modelling of the Atmosphere and Ocean,* K. Hamilton and W. Ohfuchi, Eds., Springer, 77–97.

Flament, P., S. Kennan, R. Lumpkin, M. Sawyer, and E. Stroup, 1998: The ocean. *Atlas of Hawaii,* S. P. Juvik and J. O. Juvik, Eds., University of Hawaii Press, 82–86.

Hafner, J., and S.-P. Xie, 2003: Far-field simulation of the Hawaiian wake: Sea surface temperature and orographic effects. *J. Atmos. Sci.,* **60,** 3021–3032.

Kobashi, F., and H. Kawamura, 2002: Seasonal variation and instability nature of the North Pacific Subtropical Countercurrent and the Hawaiian Lee Countercurrent. *J. Geophys. Res.,* **107,** 3185, doi:10.1029/2001JC001225.

——, S.-P. Xie, N. Iwasaka, and T. T. Sakamoto, 2008: Deep atmospheric response to the North Pacific oceanic subtropical front in spring. *J. Climate,* **21,** 5960–5975.

Komori, N., K. Takahashi, K. Komine, T. Motoi, X. Zhang, and G. Sagawa, 2005: Description of sea-ice component of coupled ocean-sea ice model for the earth simulator (OIFES). *J. Earth Simul.,* **4,** 31–45.

——, A. Kuwano-Yoshida, T. Enomoto, H. Sasaki, and W. Ohfuchi, 2008: High resolution simulation of the global coupled atmospheric-ocean system: Description and preliminary outcomes of CFES (CGCM for the Earth Simulator). *High Resolution Numerical Modelling of the Atmosphere and Ocean,* K. Hamilton and W. Ohfuchi, Eds., Springer, 241–260.

Kubota, M., N. Iwasaka, S. Kizu, M. Konda, and K. Kutsuwada, 2002: Japanese ocean flux data sets with use of remote sensing observations (J-OFURO). *J. Oceanogr.,* **58,** 213–225.

Kutsuwada, K., 1998: Impact of wind/wind-stress field in the North Pacific constructed by ADEOS/NSCAT data. *J. Oceanogr.,* **54,** 443–456.

Kuwano-Yoshida, A., T. Enomoto, and W. Ohfuchi, 2010: An improved cloud scheme for climate simulations. *Quart. J. Roy. Meteor. Soc.,* **136,** 1583–1597.

Lindzen, R. S., and S. Nigam, 1987: On the role of sea surface temperature gradients in forcing low-level winds and convergence in the tropics. *J. Atmos. Sci.,* **44,** 2418–2436.

Masumoto, Y., and Coauthors, 2004: A fifty-year eddy-resolving simulation of the world ocean: Preliminary outcomes of OFES (OGCM for the Earth Simulator). *J. Earth Simul.,* **1,** 35–56.

Maximenko, N. A., O. V. Melnichenko, P. P. Niiler, and H. Sasaki, 2008: Stationary mesoscale jet-like features in the ocean. *Geophys. Res. Lett.,* **35,** L08603, doi:10.1029/2008GL033267.

Minobe, S., A. Kuwano-Yoshida, N. Komori, S.-P. Xie, and R. J. Small, 2008: Influence of the Gulf Stream on the troposphere. *Nature,* **452,** 206–209.

Numaguti, A., M. Takahashi, T. Nakajima, and A. Sumi, 1997: Description of CCSR/NIES atmospheric general circulation model. *Study on the Climate System and Mass Transport by a Climate Model,* A. Numaguti, Ed., Center for Global Environmental Research, National Institute for Environmental Studies, 1–48.

Ohfuchi, W., and Coauthors, 2004: 10-km mesh meso-scale resolving simulations of the global atmosphere on the Earth Simulator—Preliminary outcomes of AFES (AGCM for the Earth Simulator). *J. Earth Simul.,* **1,** 8–34.

Pacanowski, R. C., and S. M. Griffies, 1999: The MOM 3 manual. GFDL Ocean Group Tech. Rep. 4, NOAA/Geophysical Fluid Dynamics Laboratory, Princeton, NJ, 680 pp.

Qiu, B., D. A. Koh, C. Lumpkin, and P. Flament, 1997: Existence and formation mechanism of the North Hawaiian Ridge Current. *J. Phys. Oceanogr.,* **27,** 431–444.

Richter, I., S. K. Behera, Y. Masumoto, B. Taguchi, N. Komori, and T. Yamagata, 2010: On the triggering of Benguela Niños: Remote equatorial versus local influences. *Geophys. Res. Lett.,* **37,** L20604, doi:10.1029/2010GL044461.

Sakamoto, T. T., A. Sumi, S. Emori, T. Nishimura, H. Hasumi, T. Suzuki, and M. Kimoto, 2004: Far-reaching effects of the Hawaiian Islands in the CCSR/NIES/FRCGC high-resolution climate model. *Geophys. Res. Lett.,* **31,** L17212, doi:10.1029/2004GL020907.

Sasaki, H., and M. Nonaka, 2006: Far-reaching Hawaiian Lee Countercurrent driven by wind-stress curl induced by warm SST band along the current. *Geophys. Res. Lett.,* **33,** L13602, doi:10.1029/2006GL026540.

——, S.-P. Xie, B. Taguchi, M. Nonaka, and Y. Masumoto, 2010: Seasonal variations of the Hawaiian Lee Countercurrent induced by the meridional migration of the Trade Winds. *Ocean Dyn.,* **60** (3), 705–715.

——, ——, ——, ——, S. Hosoda, and Y. Masumoto, 2012: Interannual variations of the Hawaiian Lee Countercurrent induced by low potential vorticity water ventilation in the subsurface. *J. Oceanogr.,* **68,** 93–111.

Seo, H., M. Jochum, R. Murtugudde, A. J. Miller, and J. O. Roads, 2007: Feedback of tropical instability-wave-induced atmospheric variability onto the ocean. *J. Climate,* **20,** 5842–5855.

Shimada, T., and S. Minobe, 2011: Global analysis of the pressure adjustment mechanism over sea surface temperature fronts using AIRS/Aqua data. *Geophys. Res. Lett.,* **38,** L06704, doi:10.1029/2010GL046625.

Small, R. J., and Coauthors, 2008: Air–sea interaction over ocean fronts and eddies. *Dyn. Atmos. Oceans,* **45,** 274–319.

Taguchi, B., R. Furue, N. Komori, A. Kuwano-Yoshida, M. Nonaka, H. Sasaki, and W. Ohfuchi, 2012a: Deep oceanic zonal jets constrained by fine-scale wind stress curls in the South Pacific Ocean: A high-resolution coupled GCM study. *Geophys. Res. Lett.,* **39,** L08602, doi:10.1029/2012GL051248.

——, H. Nakamura, M. Nonaka, N. Komori, A. Kuwano-Yoshida, K. Takaya, and A. Goto, 2012b: Seasonal evolutions of atmospheric response to decadal SST anomalies in the North Pacific subarctic frontal zone: Observations and a coupled model simulation. *J. Climate,* **25,** 111–139.

Tokinaga, H., Y. Tanimoto, S.-P. Xie, T. Sampe, H. Tomita, and H. Ichikawa, 2009: Ocean frontal effects on the vertical development of clouds over the western North Pacific: In situ and satellite observations. *J. Climate,* **22,** 4241–4260.

Uppala, S. M., and Coauthors, 2005: The ERA-40 Re-Analysis. *Quart. J. Roy. Meteor. Soc.,* **131,** 2961–3012.

Wallace, J. M., T. P. Mitchell, and C. Deser, 1989: The influence of sea surface temperature on surface wind in the eastern equatorial Pacific: Seasonal and interannual variability. *J. Climate,* **2,** 1492–1499.

Wentz, F. F., C. Gentemann, D. Smith, and D. Chelton, 2000: Satellite measurements of sea surface temperature through clouds. *Science,* **288,** 847–850.

Xie, S.-P., W. T. Liu, Q. Liu, and M. Nonaka, 2001: Far-reaching effects of the Hawaiian Islands on the Pacific ocean-atmosphere system. *Science,* **292,** 2057–2060.

Yoshida, S., B. Qiu, and P. Hacker, 2011: Low-frequency eddy modulations in the Hawaiian Lee Countercurrent: Observations and connection to the Pacific Decadal Oscillation. *J. Geophys. Res.,* **116,** C12009, doi:10.1029/2011JC007286.